Available online at www.sciencedirect.com

SciVerse ScienceDirect

Ceramics International 39 (2013) 1045–1055

CERAMICS INTERNATIONAL

www.elsevier.com/locate/ceramint

Cathodic electrodeposition of $Y(OH)_3$ and Y_2O_3 nanostructures from chloride bath. Part II: Effect of the bath temperature on the crystal structure, composition and morphology

Mustafa Aghazadeh[a,*], Abbas-Ali Malek Barmi[a,b], Hamid Mohammad Shiri[c], Sajjad Sedaghat[a]

[a]*Islamic Azad University, Malard branch, Malard, Iran*
[b]*NSTIR, P.O. Box 14395-834, Tehran, Iran*
[c]*Department of Chemistry, Payame Noor University, P. O. Box 19395-3697, Islamic Republic of Iran*

Received 21 June 2012; accepted 7 July 2012
Available online 20 July 2012

Abstract

Ultra-fine nanoparticles, mono-dispersed nanospheres and nanorods of $Y(OH)_3$ and Y_2O_3 were successfully prepared via electrodeposition from chloride bath at different temperatures of 10, 25, 40 and 80 °C followed by heat-treatments at 600 °C in dry air atmosphere. Thermal behavior of the hydroxide samples was investigated by differential scanning calorimetry (DSC) and thermogravimetric (TG) analysis. The structural and morphological characteristics of the products were determined by X-ray diffraction (XRD), FT-IR, scanning and transmission electron microscopy (SEM and TEM). Effects of bath temperature on the mechanism of base electrogeneration and deposit formation on the cathode surface were proposed and discussed. The results showed that the crystal structure, composition and morphology of the products are mainly affected by the temperature of electrodeposition bath.

Keywords: A. Calcination; A. Powders: electrochemical preparation; B. Electron microscopy; D. Y_2O_3

1. Introduction

Yttrium compounds, Y_2O_3 and $Y(OH)_3$, are important engineering materials due to their excellent chemical and physical properties, such as high permittivity, high melting point, high strength and high fracture toughness. For example, Y_2O_3 is widely used in yttrium aluminum garnets (YAG) [1,2], Eu-doped Y_2O_3 phosphors [3] and yttria stabilized zirconia (YSZ) films [4]. It could be used as a waveguide material due to its high refractive index, or as a buffer layer for ferroelectrics and superconductors because of its low lattice-mismatch with silicon [5,6]. In recent years, various physical and chemical methods such as chemical precipitation [7–9], sol–gel [10,11], combustion [12], pyrolysis [13], solvothermal [14–17] and hydrothermal [18–24] techniques have been employed for the synthesis of nanoparticles, nanotubes, nanorods, nanowires and nest-like structures of Y_2O_3 and the related compounds. Besides these methods, cathodic electrodeposition has been also applied as an attractive technique in the preparation of yttrium oxide and hydroxide thin films or coatings on various substrates [25–33]. The most successful development principle in this clean and inexpensive technique has been mentioned as a powerful control on the structural and morphological properties of the deposited films via parameters such as current density, potential, concentration, pH, temperature, surfactant and substrate type. Lee and Tak synthesized Y_2O_3 films on indium–tin-oxide (ITO) via cathodic electrodeposition of yttrium hydroxide followed by heat-treatment [26]. Zhitomirsky and Petric [27] performed cathodic deposition of Y_2O_3 from the aqueous baths of $Y(NO_3)_3$ and YCl_3 on Ni substrates and found that the amount of hydroxide deposit could be controlled by changing the current density, deposition time and yttrium salt concentration. Recently, Tondo et al.

---

[*] Corresponding author. Tel./fax: +98 21 55229204.
E-mail address: mustafa.aghazadeh@gmail.com (M. Aghazadeh).

0272-8842/$ - see front matter © 2012 Elsevier Ltd and Techna Group S.r.l. All rights reserved.
http://dx.doi.org/10.1016/j.ceramint.2012.07.026

[33] prepared Y_2O_3, Y_2O_3/Co_3O_4 and Y_2O_3/Au composite coatings on AISI 430 plates from chloride salt dissolved in hydroalcoholic solution containing chitosan as binder. However, all of these works [25–33] have mainly focused on the preparation of thin, adhesive and track-free Y_2O_3 films or coatings on various substrates without considering the structure of the obtained products at nanoscale. Thus, cathodic electrodeposition of nanostructured Y_2O_3 powder is an interesting subject to study. On the other hand, due to the nanosize dependent physico-chemical properties of metal oxides, which enhance their effective surface areas and also develop their utilization in many fields, preparation of nanostructured yttrium oxide and hydroxide is valuable. In the previous works [34–37], we applied cathodic electrodeposition for preparation of the nanostructured yttrium oxide and hydroxide powders and reported that the various nanostructures of Y_2O_3 such as nanospheres [34], nanorods [35], ultra-fine nanoparticles [36] and nanocapsules [37] are achievable by cathodic electrodeposition. For this purpose, $Y(OH)_3$ was first galvanostatically grown on the cathode via base electrogeneration. Then it was thermally converted into final oxide product via heat-treatment at 600 °C. Our studies [34,35] showed that the electrodeposition from $YCl_3 \cdot 6H_2O$ (0.01 M) bath at room temperature with applying the current densities of 2 and 0.1 mA cm^{-2} promote the formation of Y_2O_3 nanospheres and nanorods, respectively, indicating the importance of the applied current density. Also, electrodeposition from the same bath at low-temperature of 10 °C and the current densities of 0.5 and 0.1 mA cm^{-2} resulted in the $Y(OH)_3$ and Y_2O_3 ultrafine nanoparticles [36] and nanocapsules [37], respectively. However, effects of deposition conditions on the electrodeposition mechanism, and the structural and morphological properties of the products have not been systematically investigated until now. In this study, cathodic electrodeposition of Y_2O_3 was systematically carried out in a galvanostatic mode from chloride bath at different temperatures of 10, 25, 40 and 80 °C, and the effects of the bath temperature on the mechanism of base electrogeneration, and crystal structure, composition and morphology of the products were investigated.

2. Experimental procedure

2.1. Samples preparation

An additive-free 0.01 M $YCl_3 \cdot 6H_2O$ (Merck) aqueous solution was used as the electrodeposition bath. The electrochemical cell included a cathodic steel substrate (316 L, 100 × 50 × 0.5 mm^3) centered between two parallel graphite counter-electrodes. Prior to each deposition, steel substrates have given an galvanostatically electropolishing treatment at a current density of 0.5 A cm^{-2} for 5 min in a bath (70 °C) containing 50 vol% phosphoric acid, 25 vol.% sulfuric acid and balanced deionized water. All electrodeposition experiments were performed galvanostatically at a current density of 1 mA cm^{-2} for 30 min at different bath temperatures of 10, 25, 40 and 80 °C as listed in Table 1. After electrodeposition, the steel electrodes were washed several times with double-distilled water and dried at room temperature for 48 h. Then the deposits were scraped from the steel electrodes and the obtained powders were subjected to further analysis. Heat-treatment of the hydroxide powders was conducted at the temperature of 600 °C in dry air atmosphere for 3 h.

2.2. Samples characterization

The crystal structure of the prepared hydroxide and oxide samples was determined by X-ray diffraction (XRD) with a diffractometer (Phillips, PW-1800) using monochromatized Cu Kα radiation at a scanning speed of 0.5°/min. Thermal analysis of the hydroxide samples was investigated by differential calorimetric analysis (DSC, STA-1500) in air between room temperature and 600 °C at a heating rate of 5 °C min^{-1}. The surface morphology of the samples was studied using scanning electron microscopy (SEM; Philips 515, 3 kV accelerating voltage) and transmission electron microscopy (TEM; Phillips EM 2085, 100 kV accelerating voltage). IR spectra were recorded by a Bruker Vector 22 FT-IR spectrometer.

3. Results and discussion

3.1. Mechanism of deposit formation and effects of bath temperature

The deposition of yttrium hydroxide on the cathode surface from chloride medium can be explained through a two-step electrochemical–chemical (EC) mechanism as follows:

1. Electrochemical step (base electrogeneration at the cathode surface):

$$O_2+2H_2O+4e^- \rightarrow 4OH^-, \quad E^0=0.18 \text{ V vs. Ag/AgCl} \qquad (1-1)$$

Table 1
The applied electrochemical parameters in the electrodeposition experiments and samples name.

Sample name	Hydroxide Oxide	YHC-10 YOC-10	YHC-25 YOC-25	YHC-40 YOC-40	YHC-80 YOC-80
Applied current density (mA cm^{-2})	1	1	1	1	
Deposition time (min)	30	30	30	30	
Bath temperature (°C)	10	25	40	80	
Current efficiency (%)	88	83	70	61	

$$2H_2O+2e^- \rightarrow H_2+2OH^-, \quad E^0=-1.08 \text{ V vs. Ag/AgCl} \qquad (1-2)$$

2. Chemical step (deposit formation):

$$Y^{3+}(aq)^- + 3OH^-(aq) + yH_2O \rightarrow [Y(OH)_3 \times yH_2O]\downarrow \qquad (2-1)$$

$$Y^{3+}(aq)^- + (3-x)OH^-(aq) + xCl^- + yH_2O \rightarrow [Y(OH)_{(3-x)}(Cl)_x \times yH_2O]\downarrow \qquad (2-2)$$

The reactions of (1-1) and (1-2) result in the increase of local pH at the cathode surface. This process is known as electrogeneration of base. By increasing the OH^- concentration to the required conditions in the chemical step (Eq. (2-1) and (2-2)), yttrium hydroxide will form and deposit on the cathode. Fig. 1a shows the cyclic voltammetry (CV) curves of steel electrode from chloride bath with the scan rate of 30 mV s^{-1} at different temperatures of 10, 25, 40 and 80 °C. All the polarization curves (except ones recorded at temperature of 80 °C) show approximately a same profile but with differences in the potential domains. These curves can be divided into the four zones. Zone I, at the potentials higher than –0.3 V, dissolved oxygen molecules (Eq. (1-1)) is reduced and local increasing of the pH at the cathode surface occurred. This step showed lowest current density in all the curves. In next zone, fast increasing the current density is observed and potential moves to the water reduction potentials (zone II). After this stage, a steady state is observed for the current density (zone III). This phenomenon is attributed to the surface blocking by the film formed from the chemical step. In this zone, the current density is slightly lowered

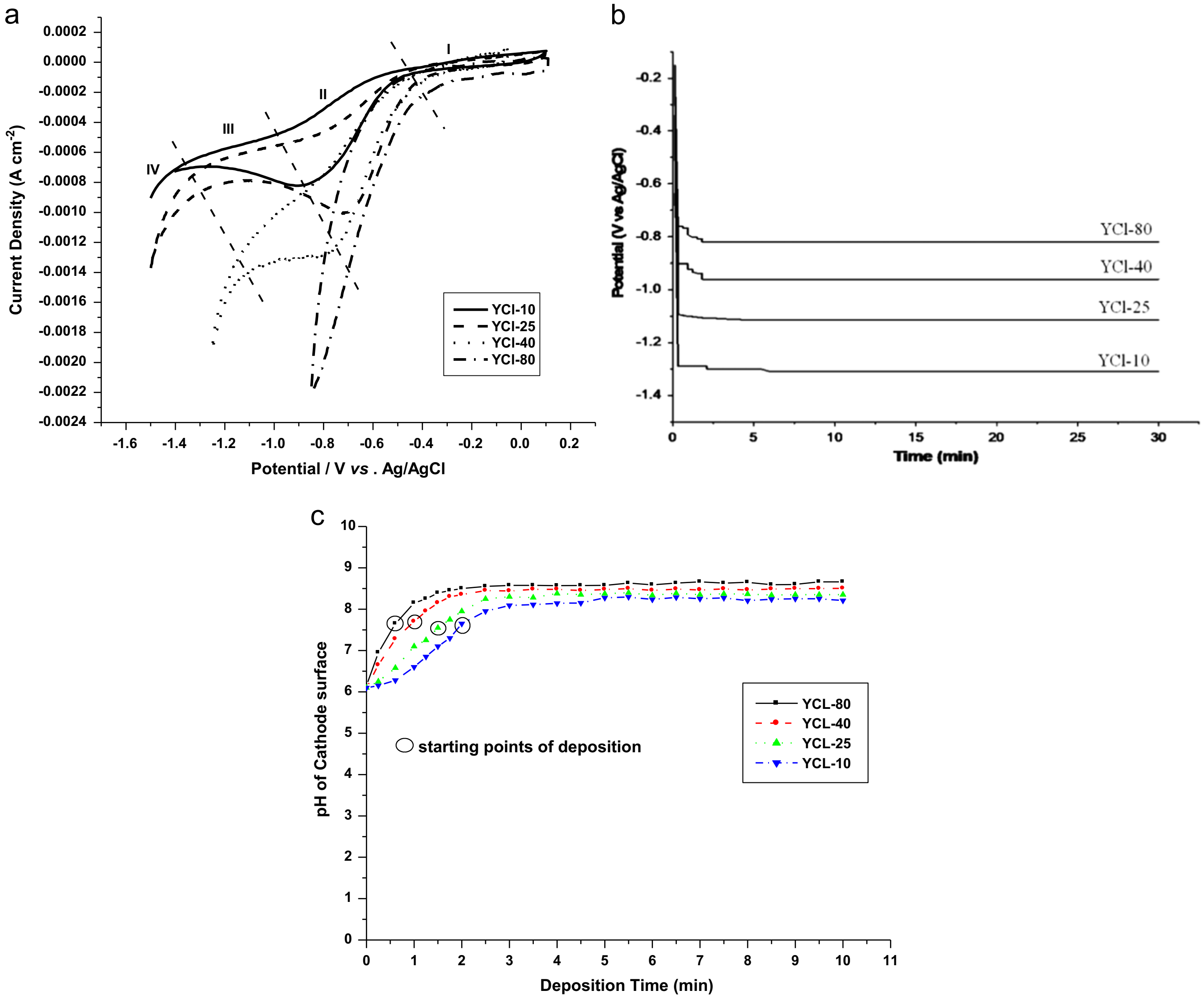

Fig. 1. (a) CV curves of the steel electrode from chloride bath at different temperatures of 10, 25, 40 and 80 °C with scan rate of 30 mV s^{-1}, and variations of the cathode potential (b) and pH (c) during the deposition experiments.

which is related to the complete blocking of the cathode surface and insulating nature of hydroxide film. Further continuation of potential scan towards the cathodic potentials results in an increase of the current density due to hydrogen evolution reaction (zone IV in Fig. 1a). At the same time, strings of H_2 gas bubbles start being observed. This feature may indicate that the film formed on the steel undergoes local breakdown manifested in gas bubbles, creating sites of stronger reduction current. At bath temperature of 80 °C, due to the reduced hydrogen evolution potential i.e. H_2 overpotential at the steel surface, the water reduction and H_2 bubbling occurred at higher potentials. As a result, reduction active sites always exist on the cathode surface and the steel surface is not completely blocked by the hydroxide film. Thus, it is expected that no film formation zone (zone III) be observed in the polarization curve of 80 °C (as seen in the Fig. 1a). Fig. 1b shows variations of the potential during the electrodeposition of $Y(OH)_3$ at different bath temperatures. The potential values suggest that the reduction of water (Eq. (1-2)) has a major role in the production of OH^- at all the applied deposition conditions. The hydrogen evolution can make a unique porous structure and preferred growth at a certain direction. Thus it can be said that morphology of the products will be affected by bath temperature.

The bath temperature affects the kinetic of the involved reactions, diffusion velocity of ions and interfacial pH. These changes could be explained by considering the $Y(OH)_3$ precipitation, bath temperature and solubility constant K_s, which they are theoretically linked by the Van't Hoff relation:

$$\frac{d\ln K_S}{dT} = \frac{\Delta H^o}{RT^2} \tag{3}$$

where ΔH^0 is the standard enthalpy of dissolution of $Y(OH)_3$. So taking into account that the dissolution ΔH^0 term in relation (3) is low in general, K_s is considered constant, as a rough approximation. Then from the set of relations at constant temperature,

$$K_S = [Y^{3+}][OH^-]^3 \tag{4}$$

$$K_W = [H_3O^+][OH^-] \tag{5}$$

following relation is obtained:

$$\frac{1}{[H_3O^+]}] = \frac{1}{K_W}\left(\frac{K_S}{[Y^{3+}]}\right)^{1/3} \tag{6}$$

The expression of the interfacial pH for starting precipitation (pH_{st}) becomes

$$pH_{st} = pH_e + \text{constant} \tag{7}$$

This relation shows that the bath temperature has theoretically a continuous influence on pH_{st} [38], as a result the facility to form the final deposit mass. In fact, bath temperature seems to influence the change in the deposition reactions. Fig. 1c shows variations of the pH on the cathode surface during the electrodeposition of $Y(OH)_3$ at different bath temperatures. These curves clearly indicate that pH at the cathode surface is quickly increased at initial times of the deposition process due to base electrogeneration in the electrochemical step (reactions of (1-1)). It is worth noting that the rate of base generation at the elevated bath temperatures is higher compared with the lower temperatures, as one can obviously see from the slope of the pH curves in Fig. 1c. With increasing the pH at the cathode surface at longer deposition times, the conditions for the chemical step are ready and yttrium hydroxide starts to form and deposit on the cathode surface. Considering the solubility constant of $Y(OH)_3$ ($K_{sp}=[Y^{3+}][OH^-]^3=10^{-22.1}$), it is expected that the yttrium hydroxide will deposit from the 0.01 M aqueous solution of $YCl_3 \cdot 6H_2O$ at pH of about 7.3. In fact, at this time of deposition, the OH^- produced from the electrochemical step has started to be consumed in the chemical step. Deposit formation via the reaction of (2-1) can result in the intercalation of chloride ions in the deposit structure. Thus the $Y(OH)_3$ and/or $Y(OH)_{(3-x)}Cl_x$ composition is expected for the obtained deposits (as confirmed by XRD and TG analyses). From Fig. 1c, it can be seen that the chemical step was approximately started at the times of 37, 58, 93 and 136 s after the starting of the experiments (starting points of deposition). After these points, the electrogenerated base in the electrochemical step is subsequently consumed at the chemical step. As a result, the slope of the pH curves is lowered and then it

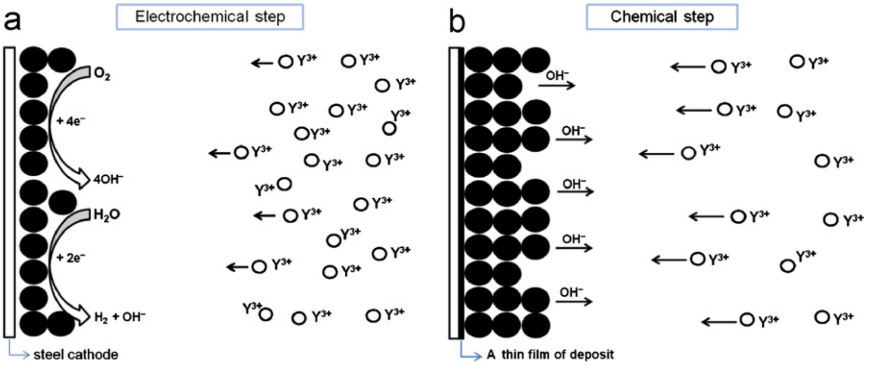

Fig. 2. Schematic view of the electrochemical (a) and chemical (b) steps in the cathodic electrodeposition of $Y(OH)_3$ from chloride bath.

approximately remained constant (as seen in Fig. 1c). However, the level of pH on the cathode surface is mainly determined by the applied bath temperature. These findings clearly indicate the direct effects of bath temperature on the base electrogeneration and deposit formation, which are in agreement with the theoretical calculations (Eq. 7). The electrochemical (a) and chemical (b) steps during the $Y(OH)_3$ electrodeposition from chloride bath are schematically shown in Fig. 2.

3.2. Thermal behavior of samples

To explore the mechanism of oxide formation during the heat-treatment process, thermal behaviors of the prepared $Y(OH)_3$ powders were examined by differential scanning calorimetry. The DSC and related TG curves are shown in Fig. 3. The DSC curves in Fig. 3a show that all the samples have approximately the same thermal behaviors. These curves also exhibit three distinct endothermic peaks with maximums at about 100, 415 and 485 °C for all the samples, indicating the three successive stages of physicochemical changes and oxide formation during the heat-treatment (Fig. 3a). For all samples, the low temperature endothermic peaks at temperatures less than 150 °C are related to the dehydration of free and physically absorbed water molecules associated with the prepared powders. Accordingly, the TG curves show weight losses at this range of temperature, based on the below reaction (section 1 in Fig. 3b):

$$[Y(OH)_{(3-x)}(Cl)_x\cdot yH_2O]\xrightarrow{25-150\,^{\circ}C}[Y(OH)_{(3-x)}(Cl)_x]+yH_2O \tag{8}$$

In the literature [39,40], the temperature of chloride removal from the deposit structure has been reported in the range of 300–450 °C. On the other hand, it has been

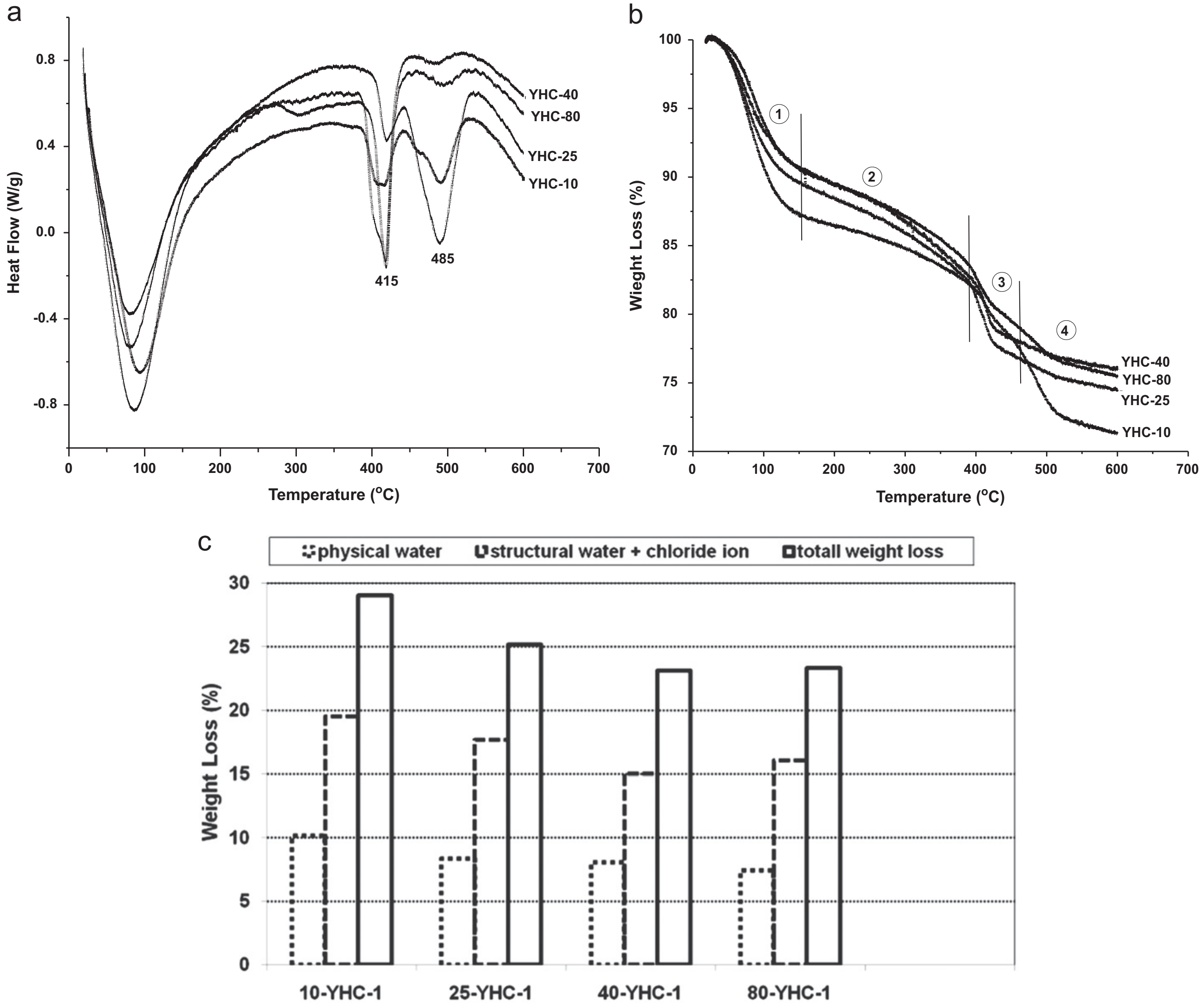

Fig. 3. DSC (a) and related TG (b) curves of the prepared hydroxide samples at different bath temperatures, and (c) the observed weight losses in TG curves.

found that the initially formed hydroxide phase transforms into α-Y(OH)$_3$ at about 350 °C [26,34]. It is also reported that the initially formed deposit is transformed to the yttrium oxyhydroxide at 400–450 °C [35]. Thus, the following changes can be proposed for the peaks observed at the temperatures 200–450 °C:

$$[Y(\mathrm{OH})_{(3-x)}(\mathrm{Cl})_x] \xrightarrow{150-400\,^\circ\mathrm{C}} [\alpha\text{-}Y(\mathrm{OH})_{(3-x)}(\mathrm{Cl})_x] \quad (9)$$

$$[\alpha\text{-}Y(\mathrm{OH})_{(3-x)}(\mathrm{Cl})_x] \rightarrow [\mathrm{YO(OH)}_{(1-x)}] + x\mathrm{HCl} + \mathrm{H_2O} \quad (10)$$

These conformations are seen at the XRD patterns, where the patterns in Fig. 3b showed the α-Y(OH)$_3$ and YOOH diffraction peaks at this range of temperature. From the results of TG analysis in Fig. 3c, it is seen that the chloride ions have enough time for intercalation in the deposit structure at lower applied current densities, probably due to the slow kinetics of base electrogeneration and deposit formation. The sharp weight loss at the range of 400–450 °C is related to the removal of structural water associated intercalated chloride ions in the deposit structure, which leads to conformation from yttrium hydroxide into oxyhydroxide (section 3 in Fig. 3b). The last endothermic peaks at 500 °C for all samples show the complete removal of the structural water and the formation of well-crystallized final oxide product:

$$[\mathrm{YO(OH)}_{(1-x)}] + 1/2\mathrm{O_2} \rightarrow \mathrm{Y_2O_3} + (1-x)\mathrm{H_2O} \quad (11)$$

This transformation is also supported by the XRD (Fig. 4c) which the patterns exhibited the crystalline cubic phase of Y$_2$O$_3$ at 600 °C. Fig. 3c shows the weight losses related to the dehydration of physical and structural water, and removal of the intercalated chloride ions from the hydroxide samples. Physically absorbed water shows a direct trend with the applied bath temperature. In fact, water molecules are better absorbed on the deposit structure at lower temperatures. On the other hand, chloride ions are also better intercalated at lower bath temperatures (as seen from Fig. 3c). It seems that there is a competition between the water molecules and chloride ions for intercalation in the deposit structure. At higher bath temperatures, the chloride ions cannot intercalate in the deposit structure due to the intensive water reduction and evolution of H$_2$ bubbles on the cathode surface. The H$_2$ bubbles may act as a barrier layer on the reaching of the chloride ions to the cathode surface. Finally, from Fig. 3c, it can be seen that there is no special trend for total weight loss with bath temperature.

3.3. Crystal structure of the samples

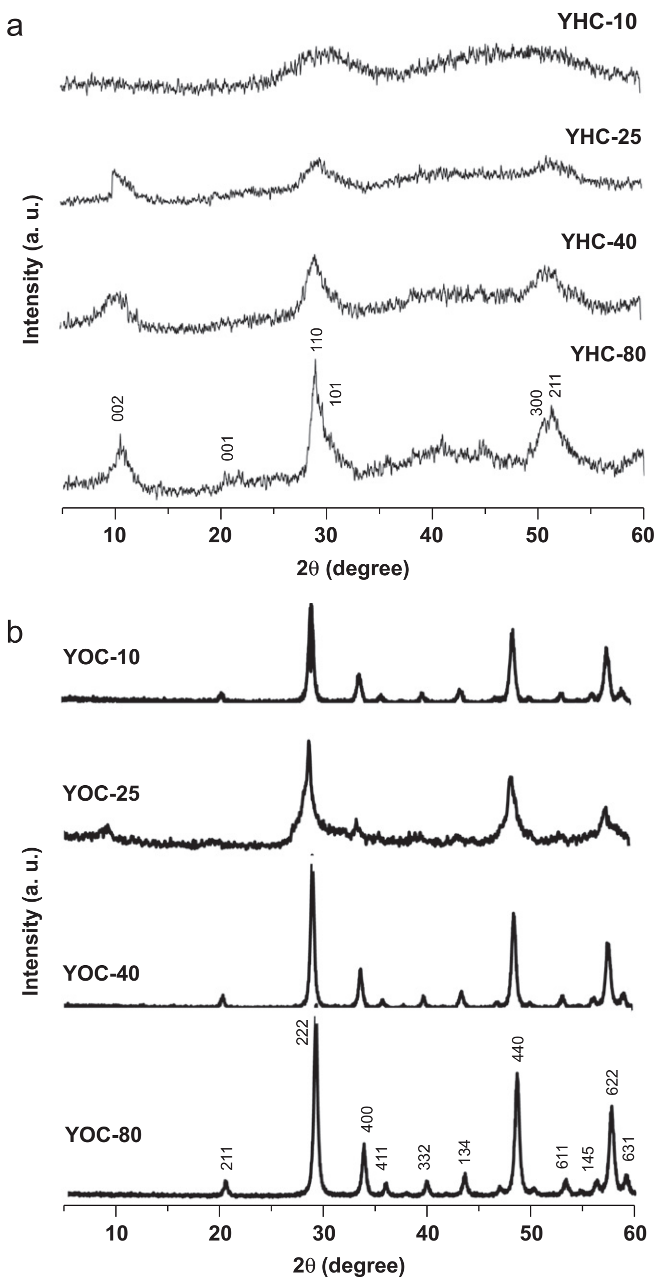

Fig. 4. XRD patterns of the prepared (a) hydroxide and (b) oxide samples at different bath temperatures of 10, 25, 40 and 80 °C.

The XRD patterns of the prepared hydroxide and oxide samples are shown in Fig. 4. The hydroxide samples prepared at lower temperatures (YHC-10 and YHC-25) exhibits two very broad peaks near $2\theta = 30^\circ$ and 55°, which can be regarded as an amorphous or poorly crystallized yttrium hydroxide. The broadening of diffraction peaks in the patterns indicates that the crystal size of YHC-10 and YHC-25 samples is fine (as confirmed by SEM and TEM images). From the XRD patterns of the hydroxide samples (Fig. 4a), it is clearly seen that the diffraction peaks come sharp and new peaks are formed with increasing of the bath temperature. These changes indicate that the deposit is well crystallized at higher bath temperatures. It seems that the bath temperature affects the nucleation and growth of the deposit as well as base electrogeneration reactions as mentioned above. All diffraction peaks except (001) and (002) in XRD pattern of YHC-80 (Fig. 4a) can be assigned to the hexagonal phase of the Y(OH)$_3$ (JCPDS Card no. 21-4547). Based on Ref. [41], it can be said that the (001) and (002) peaks have resulted from the intercalation of chloride ions in the deposit structure during the deposition process. It is worth noting that the XRD patterns of the samples prepared at lower temperatures show a small broad peak at $2\theta = 10°$, which can be resulting from chloride intercalation in the deposit structure. It is also clearly seen that the bath temperature has a major effect on the crystal structure of the hydroxide deposits. For the heat-treated samples, the XRD patterns in Fig. 4b show a marked increase in the peak intensity and the formation of new peaks, as well as a decrease in the peak width, confirming the process of phase transformations into yttrium oxide. All patterns of the oxide products can be readily indexed to a pure cubic phase of Y_2O_3 (space group Ia3/(206 1)) with a lattice constant of $\alpha = 1.06$ nm (JCPDS 25-1200). The XRD patterns of the samples show completely sharp peaks with difference in their intensities. It seems that heat-treatment process could compensate the effects of bath temperature where all oxide samples show sharp peaks. Finally, it can be concluded that the bath temperature has a major effect on the crystal structure of the prepared hydroxides.

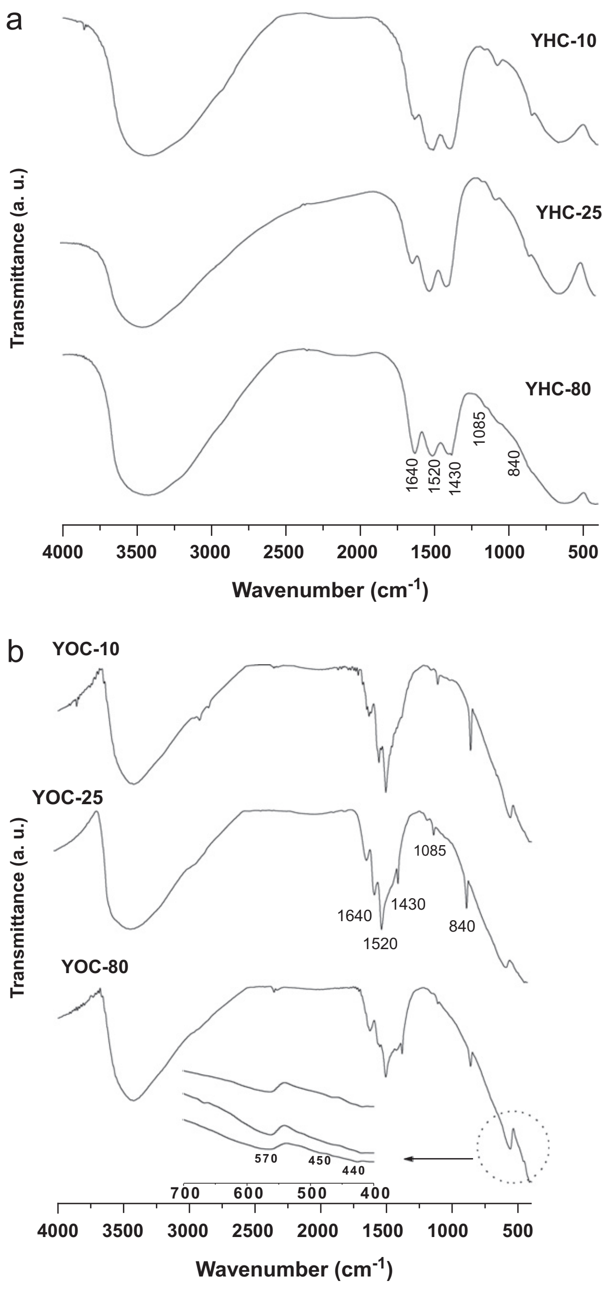

Fig. 5. IR spectra of the prepared (a) hydroxide and (b) oxide samples.

3.4. Spectral analysis

The IR spectra of the $Y(OH)_3$ and Y_2O_3 products are shown in Fig. 5 and the peak positions and their characteristics are listed in Table 2. From the IR spectra, some important points can be detected which are listed below:

- IR analysis confirmed the existence of physically adsorbed water in the hydroxide samples which is completely in agreement with the results of TG analysis.
- The peaks related to the physically adsorbed water are also seen in the oxide samples due to the moisture absorption during the testing.
- The peaks related to carbonate group stretching are observed in all the samples due to the CO_2 absorption during the testing.
- The IR spectra are completely confirming the hydroxide and oxide nature of the prepared samples.

3.5. Morphological characterization

Figs. 6–9 show the surface morphology of the yttrium hydroxide and oxide samples prepared at different bath temperatures. The SEM images (Fig. 6a and b) show the smooth and uniform surface morphology of the sample prepared at bath temperature of 10 °C (YHC-10 and YOC-

Table 2
Origin of the IR absorption bands in the hydroxide and oxide samples.

Origin	Wave number (cm^{-1}) and intensity[a]	Modes of vibration
Physically adsorbed water	3460–3470 (s)1630–1640 (s)	H–O–H stretchingH–O–H bending
CO_2 absorption from atmosphere	1520–1525 (m)1395 (w)1070–1075 (w)855–860 (w)	Carbonate group stretchingCarbonate group stretchingCO symmetric stretchingCO deformation
$Y(OH)_3$	670 (s) and 470 (s)	Y–O–H stretching
Y_2O_3	650 (s) and 425 (m)	Y–O–Y stretching

[a] s: strong peak, w: weak peak and m: middle strong peak.

10). However, due to the ultrafine size of both samples particles, more information could not be detected from the SEM images. High magnification by TEM (Fig. 6c and d) revealed that the YHC-10 and YOC-10 samples are composed of well-dispersed ultrafine particles with the sizes of smaller than 5 nm. In fact, these two samples are composed of ultrafine particles which are well-dispersed without aggregation. These results indicate that the ultrafine nanoparticles of $Y(OH)_3$ and Y_2O_3 are achievable at low-temperature chloride bath. For hydroxide sample prepared

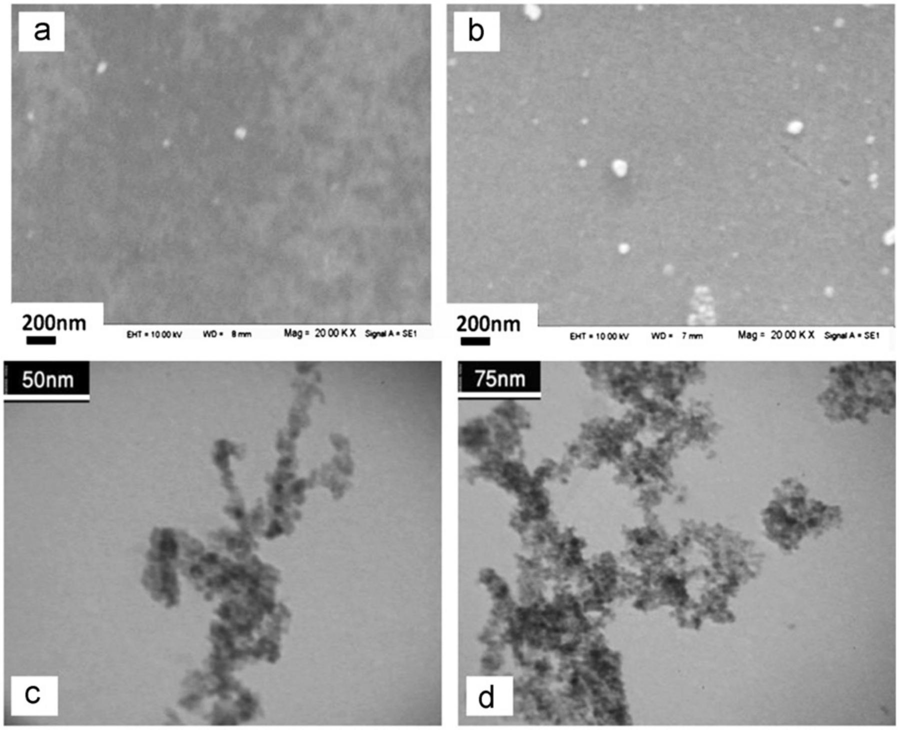

Fig. 6. SEM (a,b) and TEM (c,d) images of the YHC-10 and YOC-10 samples, respectively.

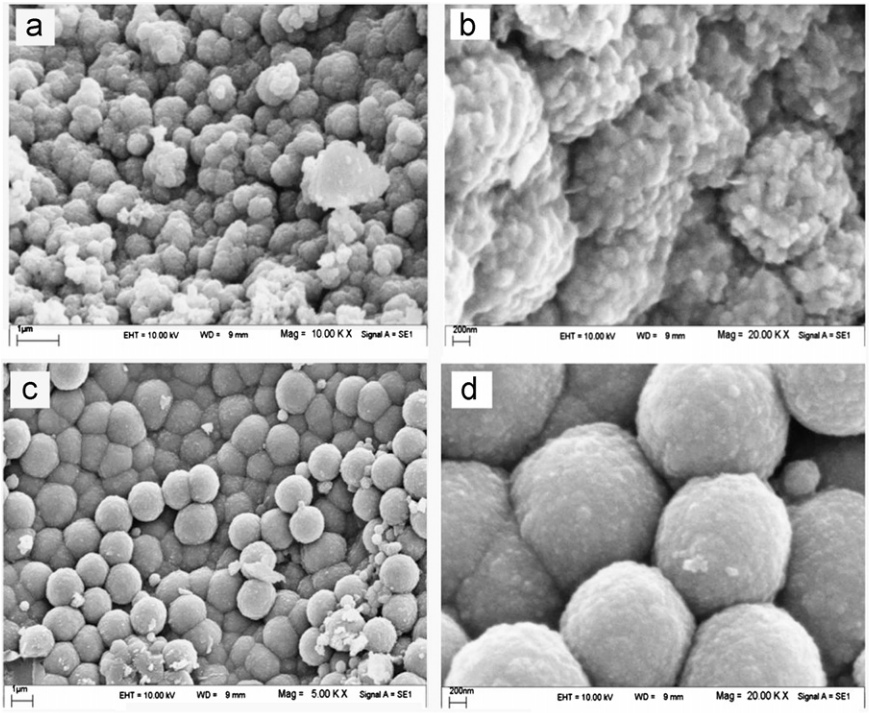

Fig. 7. SEM images of the (a,b) YHC-25 and (c,d) YOC-25 samples.

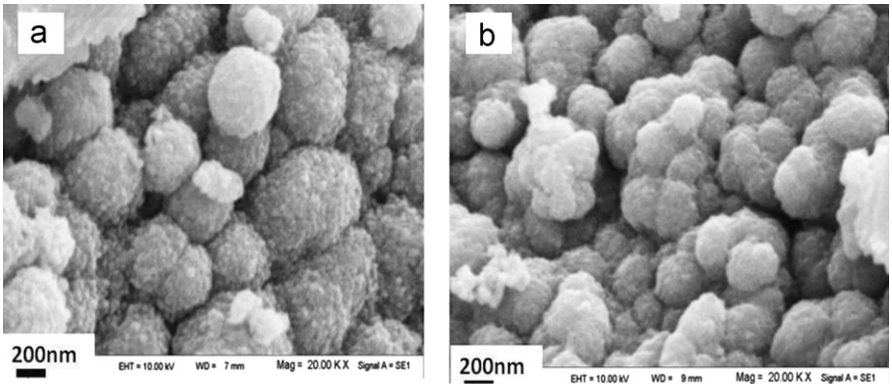

Fig. 8. SEM images of the (a) YHC-40 and (b) YOC-40 samples.

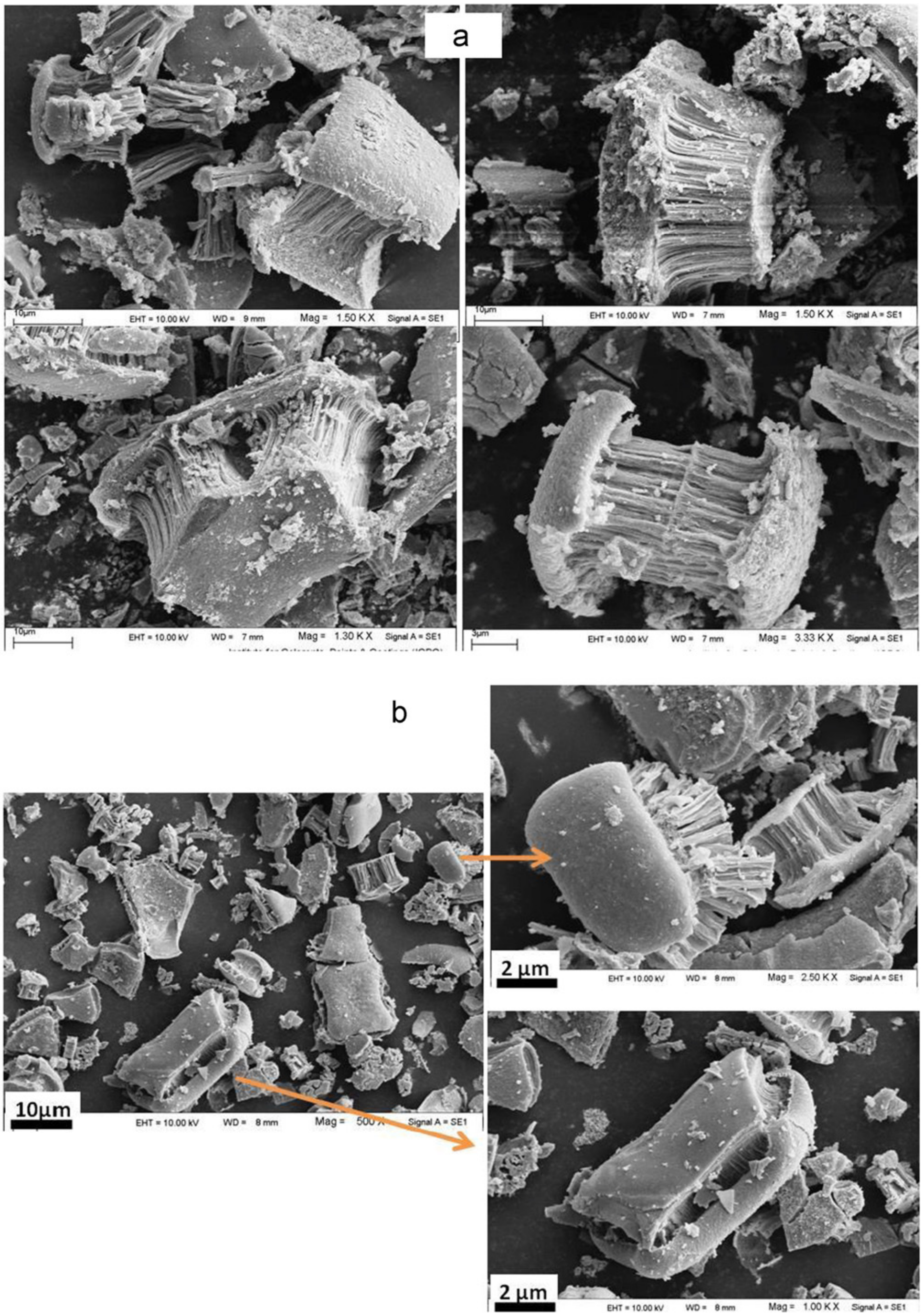

Fig. 9. SEM images of the (a) YHC-80 and (b) YOC-80 samples.

at 25 °C (YHC-25), the rough and uneven structure is seen in the SEM image (Fig. 7a), which is similar to cauliflower texture. In fact, this structure is composed of agglomerates of interconnected spherical grains. At a higher magnification, the clusters of globules with void space in between can be seen clearly (Fig. 7b). After annealing of YHC-25 at 600 °C, mono-dispersed oxide particles were obtained (Fig. 7c and d). The YOC-25 sample is composed of well-dispersed spherical particles with the average diameter of 500 nm (Fig. 7c). The observed changes in morphology may be caused by removal of incorporated electrolyte and chemisorbed water accompanied with structural transformation occurring during heat-treatment (as justified by TG and XRD analyses). The SEM images exhibit sphere-like morphology for the samples prepared at bath temperature of 40 °C (Fig. 8a and b). After annealing at 600 °C, surface of the spheres of oxide sample (YOC-40); becomes rather smooth compared with its hydroxide precursor (YHC-40), however, the oxide spheres are still agglomerated (Fig. 8b). From these observations, the bath temperature of 25 °C and current density of $-1\,\mathrm{mA\,cm^{-2}}$ can be selected for the preparation of the homogeneous and well-dispersed nanospheres of Y_2O_3. Fig. 9 shows the surface morphology of the hydroxide and oxide samples prepared at temperature of 80 °C. A completely different morphology is seen in the SEM images for these samples (Fig. 9). These samples are made up of rods, which have grown directly on the cathode surface and completely compacted together to form a package. The rods have the same length and diameter. But, the packages have completely different sizes. In fact, YHC-80 and YOC-80 samples are composed of rods packages with different sizes. This type of morphology can be related to the intensive H_2 bubbling on the cathode surface at elevated temperature of 80 °C.

Finally, it can be concluded that the bath temperature can be recognized as a main determining factor in the cathodic electrodeposition of Y_2O_3, where the morphology and crystal structure of the products are directly affected by the bath temperature.

4. Conclusion

Cathodic electrodeposition of Y_2O_3 was performed from chloride bath at different temperatures of 10, 25, 40 and 80 °C. For this purpose, $Y(OH)_3$ was firstly electrodeposited on steel substrate via base electrogeneration and then converted into oxide by heat-treatment at 600 °C. Thermal behavior of hydroxide samples during the heat-treatment was analyzed by DSC–TGA. The effects of the bath temperature on the base electrogeneration reactions, products composition, crystal structure and morphology were investigated. The results showed that the ultra-fine nanoparticles, nanospheres and nanorods of $Y(OH)_3$ and Y_2O_3 can be easily prepared at bath temperatures of 10, 25, 40 and 80 °C, respectively.

References

[1] L. Wang, H. Kou, Y. Zeng, J. Li, Y. Pan, X. Sun, J. Guo, The effect of precipitant concentration on the formation procedure of yttrium aluminum garnet (YAG) phase original, Ceramics International 38 (2012) 3763–3771.

[2] K. Laishram, R. Mann, N. Malhan, Single step synthesis of yttrium aluminum garnet ($Y_3Al_5O_{12}$) nanopowders by mixed fuel solution combustion approach, Ceramics International 37 (2011) 3743–3746.

[3] F.W. Liu, C.H. Hsu, F.S. Chen, C.H. Lu, Microwave-assisted solvothermal preparation and photoluminescence properties of Y_2O_3:Eu^{3+} phosphors, Ceramics International 38 (2012) 1577–1584.

[4] Q. Li, Y.F. Zhang, X.F. Ma, J. Meng, X.Q. Cao, High-pressure sintered yttria stabilized zirconia ceramics, Ceramics International 35 (2009) 453–456.

[5] T.T. Van, J.P. Chang, Controlled erbium incorporation and photoluminescence of Er-doped Y_2O_3, Applied Physics Letters 87 (2005) 011907–011909.

[6] B.J.H. Stadler, M. Oliver, Sputter-deposited yttria–alumina thin films for optical waveguiding, Journal of Applied Physics 84 (1998) 93–99.

[7] H. Gong, D.Y. Tang, H. Huang, T.S. Zhang, J. Ma, Effect of grain size on the sinterability of yttria nanopowders synthesized by carbonate-precipitation process, Materials Chemistry and Physics 112 (2008) 423–426.

[8] M.D. Fokema, E. Chiu, J.Y. Ying, Synthesis and characterization of nanocrystalline yttrium oxide prepared with tetraalkylammonium hydroxides, Langmuir 16 (2000) 3154–3159.

[9] Y. Huang, D. Jiang, J. Zhang, Q. Lin, Z. Huang, Synthesis of monodispersed spherical Nd:Y_2O_3 powder for transparent ceramics, Ceramics International 37 (2011) 3523–3529.

[10] C.Y. Tsay, C.H. Cheng, Y.W. Wang, Properties of transparent yttrium oxide dielectric films prepared by sol–gel process, Ceramics International 38 (2012) 1677–1682.

[11] C. Lin, C. Zhang, J. Lin, Sol–gel derived Y_2O_3 as an efficient bluish-white phosphor without metal activator ions, Journal of Luminescence 129 (2009) 1469–1474.

[12] J. Li, Y. Pan, F. Qiu, Y. Wu, W. Liu, J. Guo, Synthesis of nanosized Nd:YAG powders via gel combustion, Ceramics International 33 (2007) 1047–1052.

[13] S.Y. Wang, Z.H. Lu, Preparation of Y_2O_3 thin films deposited by pulse ultrasonic spray pyrolysis, Materials Chemistry and Physics 78 (2003) 542–545.

[14] C. Feldmann, J. Merikhi, Synthesis and characterization of rod-like Y_2O_3 and Y_2O_3:Eu^{3+}, Journal of Materials Science 38 (2003) 1731–1735.

[15] S.J. Wang, S.L. Zhong, $Y(OH)_3$ and Y_2O_3 with novel structures: formation and mechanism, Materials Science and Engineering 162B (2009) 200–204.

[16] J. Yang, Z. Quan, D. Kong, X. Liu, J. Lin, Y_2O_3: Eu^{3+} microspheres: solvothermal synthesis and luminescence properties, Crystal Growth and Design 7 (2007) 730–735.

[17] T. Yan, D. Zhang, L. Shi, H. Yang, H. Mai, J. Fang, Reflux synthesis, formation mechanism, and photoluminescence performance of monodisperse Y_2O_3:Eu^{3+} nanospheres, Materials Chemistry and Physics 117 (2009) 234–243.

[18] C. Hu, Z. Gao, Synthesis of Y_2O_3 with nestlike structures, Journal of Materials Science 41 (2006) 6126–6129.

[19] N. Li, K. Yanagisawa, N. Kumada, Facile hydrothermal synthesis of yttrium hydroxide nanowires, Crystal Growth and Design 9 (2009) 978–981.

[20] N. Li, K. Yanagisawa, Controlling the morphology of yttrium oxide through different precursors synthesized by hydrothermal method, Journal of Solid State Chemistry 181 (2008) 1738–1743.

[21] H. Zhu, Y. Ma, H. Yang, P. Zhu, J. Du, C. Ji, D. Hou, Ultrastable structure and luminescence properties of Y_2O_3 nanotubes, Solid State Communications 150 (2010) 1208–1212.

[22] J. Zhang, Z. Liu, J. Lin, J. Fang, Y_2O_3 microprisms with trilobal cross section, Crystal Growth and Design 5 (2005) 1527–1530.

[23] L. Li, H.K. Yang, B.K. Moon, B.C. Choi, J.H. Jeong, K.H. Kim, Photoluminescent properties of Ln_2O_3:Eu^{3+} (Ln=Y, Lu and Gd)

prepared by hydrothermal process and sol–gel method, Materials Chemistry and Physics 119 (2010) 471–477.

[24] S. Zhong, S. Wang, H. Xu, Spindlelike Y_2O_3:Eu^{3+} nanorod bundles: hydrothermal synthesis and photoluminescence properties, Journal of Materials Science 44 (2009) 3687–3693.

[25] Y. Matsuda, K. Imahashi, N. Yoshimoto, M. Morita, M. Haga, Formation of yttrium oxide by electrodeposition in organic electrolyte, Journal of Alloys and Compounds 193 (1993) 277–279.

[26] J. Lee, Y. Tak, Preparation of yttrium oxide film deposited by electrochemical method, Journal of Industrial and Engineering Chemistry 5 (1999) 139–142.

[27] I. Zhitomirsky, A. Petric, Electrochemical deposition of yttrium oxide, Journal of Materials Chemistry 10 (2000) 1215–1218.

[28] I. Zhitomirsky, A. Petric, Electrolytic deposition of ZrO_2–Y_2O_3 films, Materials Letters 50 (2001) 189–193.

[29] I. Avramova, D. Stoychev, T. Marinova, Characterization of a thin CeO_2–ZrO_2–Y_2O_3 films electrochemical deposited on stainless steel, Applied Surface Science 253 (2006) 1365–1370.

[30] R. Siab, G. Bonnet, J.M. Brossard, J. Balmain, J.F. Dinhut, Effect of an electrodeposited yttrium containing thin film on the high-temperature oxidation behaviour of TA6V alloy, Applied Surface Science 253 (2007) 3425–3431.

[31] C.T. Hsu, S.K. Yen, Electrolytic Y_2O_3 coating on IN617 superalloy, Journal of Electrochemical Society 152 (2005) C813–C816.

[32] C.T. Hsu, C.F. Li, S.K. Yen, Effects of electrolytic Y_2O_3 and YAG coatings on oxidation and corrosion of IN617 superalloy, Journal of Electrochemical Society 156 (2009) D11–D16.

[33] E. Tondo, M. Boniardi, D. Cannoletta, M.F. De Riccardisc, B. Bozzin, Electrodeposition of yttria/cobalt oxide and yttria/gold coatings onto ferritic stainless steel for SOFC interconnects, Journal of Power Sources 195 (2010) 4772–4778.

[34] M. Aghazadeh, A. Nozad Golikand, H. Adelkhani, M. Ghaemi, Synthesis of Y_2O_3 nanospheres via heat-treatment of cathodically grown $Y(OH)_3$ in chloride medium, Journal of Electrochemical Society 157 (2010) D519–D522.

[35] M. Aghazadeh, M. Ghaemi, A. Nozad Golikand, A. Ahmadi, Porous network of Y_2O_3 nanorods prepared by electrogeneration of base in chloride medium, Materials Letters 65 (2011) 2545–2548.

[36] M. Aghazadeh, M. Ghaemi, A. Nozad Golikand, T. Yousefi, Low-temperature electrochemical synthesis and characterization of ultra-fine $Y(OH)_3$ and Y_2O_3 nanoparticles, Journal of Rare Earths 30 (2012) 236–240.

[37] T. Yousefi, M. Aghazadeh, A. Nozad Golikand, M.H. Mashadizadeh, A new-type nanostructure of $Y(OH)_3$ prepared by electrodeposition from chloride medium via electrogeneration of base, Science of Advanced Materials 4 (2012) 214–218.

[38] D.R. Lide (Ed.), Handbook of Chemistry and Physics, 2000.

[39] L. Nan, Y. Kazumichi, Controlling the morphology of yttrium oxide through different precursors synthesized by hydrothermal method, Journal of Solid State Chemistry 181 (2008) 1738–1743.

[40] B.J. Michel, B. Josseline, C. Juan, B. Gilles, Characterization of thin solid films containing yttrium formed by electrogeneration of base for high temperature corrosion applications, Surface and Coatings Technology 185 (2004) 275–282.

[41] L. McIntyre, L. Jackson, A. Fogg, Synthesis and crystal structures of new lanthanide hydroxyhalide anion exchange materials, $Ln_2(OH)_5X \cdot 1.5H_2O$ (X=Cl, Br; Ln=Y, Dy, Er, Yb), Chemistry of Materials 20 (2008) 7447–7453.